

Inversely Designed Second-Order Photonic Topological Insulator With Multiband Corner States

Yafeng Chen,^{1,2} Zhihao Lan,^{3,*} and Jie Zhu^{4,2,†}

¹*State Key Laboratory of Advanced Design and Manufacturing for Vehicle Body, Hunan University, Changsha, Hunan 410082, China*

²*Department of Mechanical Engineering, The Hong Kong Polytechnic University, Hung Hom, Kowloon, Hong Kong SAR, China*

³*Department of Electronic and Electrical Engineering, University College London, London WC1E 7JE, United Kingdom*

⁴*School of Physics Science and Engineering, Tongji University, Shanghai 200092, China*

(Received 17 January 2022; revised 20 March 2022; accepted 14 April 2022; published 2 May 2022)

Second-order photonic topological insulators (SPTIs) with topologically protected corner states possess extraordinary abilities of robust light steering in lower dimensions. However, previous SPTIs are difficult for multiband on-chip applications. To overcome this challenge, we design, via the inverse design method, a SPTI supporting four highly localized corner states within four sizeable band gaps that are robust to bulk impurities. Importantly, the designed SPTI is made of fully connected dielectric materials, which can be readily fabricated in nanoscale via electron-beam lithography and integrated into on-chip circuits. Our work offers potential applications in designing multiband on-chip photonic integrated devices with high efficiency, high capacity, and high robustness for both linear and nonlinear optical processing.

DOI: 10.1103/PhysRevApplied.17.054003

I. INTRODUCTION

Photonic topological insulators (PTIs) are systems that host topological boundary states protected against impurities in the bulk, offering great opportunities for achieving the robust steering of light [1]. To date, obeying the bulk-boundary correspondence principle, PTIs based on quantum Hall effect [2,3], quantum spin Hall effect [4–6], and quantum valley Hall effect [7–11] have been achieved. These PTIs are characterized by the gapless edge states that are one-dimensional (1D) lower than the bulk. Meanwhile, toward multiband applications, a PTI supporting dual-band valley edge states has been demonstrated [12,13].

Recently, a class of high-order PTI that supports lower-dimensional topological boundary states has been achieved [14], which goes beyond the conventional bulk-boundary correspondence. In the two-dimensional (2D) system, the so-called second-order PTI (SPTI) hosts 1D gapped edge states and 0D in-gap corner states. Crystalline symmetry is crucial for engineering the SPTI. Hitherto, several versions of SPTIs have been realized based on different symmetric lattices, e.g., C_{6v} - and C_3 -symmetric hexagonal lattice [15–17], C_{3v} -symmetric kagome lattice [18], and C_{4v} -symmetric square lattice [19–24]. As the energies

are tightly localized at the corners, SPTIs could enhance the light-matter interaction, thus having promising applications in linear and nonlinear integrated optics. To date, based on the SPTI, topological nanocavity with high quality factor [25], topological insulator lasers [26,27], and topologically enhanced nonlinear frequency conversion [28,29] have been demonstrated. However, most previous SPTIs only support corner states within one band gap, limiting multiband applications, e.g., multiband lasers [30], multiband resonators [31], multiband filters [32], and so forth. Most recently, multiband valley bands and second-order corner states have been demonstrated in a 2D SPTI for the transverse magnetic (TM) mode [33]. However, the proposed SPTI is made of isolated pillars, which is difficult to manufacture at the nanoscale and inconvenient for integration into on-chip photonic circuits.

To overcome this challenge, with the aid of the inverse design technique, we herein design a multiband SPTI made of fully connected dielectric materials in which four topological corner states within four wide band gaps are observed. The robustness of these corner states against defects is further demonstrated. The designed SPTI can be readily fabricated via electron-beam lithography technology and integrated into photonic circuits [7,11,34–36], which can find potential applications in linear and nonlinear on-chip photonic devices.

* z.lan@ucl.ac.uk

† jiezhu@tongji.edu.cn

II. RESULTS AND DISCUSSION

To design the SPTI made of connected dielectric materials for integrated optics applications, we focus on the transverse electric (TE) modes herein [37], where the magnetic field is perpendicular to the propagation plane. We consider a 2D photonic crystal (PC) with C_{4v} symmetry, which is made of silicon with permittivity of $\epsilon = 12.25$. As a band gap is the prerequisite for the existence of corner states, to design the SPTI hosting multiband corner states, we first adopt the topology optimization technique, bidirectional evolutionary structure optimization (BESO) algorithm [38], to design the PC with multiple band gaps. Totally, four band gaps at four target frequencies are assigned. The detailed description of the topology optimization approach is presented in Appendix A. The whole optimization process takes about two to three hours on a computer with an Intel i7-6700HQ (2.6 GHz) CPU and 8GB RAM. Note that the optimized structure obtained in this paper may be not the global optimum solution as our numerical experience indicates that a different initial structure could result in different solutions. For the brevity of analysis, the frequency is normalized as a/λ , where λ is the wavelength and a the lattice constant. Figure 1(a) shows the optimized PC with the primitive unit cell (UC) denoted by the red dashed box. One can see that the dielectric materials are fully connected without isolated pillars; thus the structure can be readily fabricated using the method of electron-beam lithography [7,11,34–36]. From the band diagram shown in Fig. 1(b), four band gaps (labeled as I, II, III, and IV, respectively) are observed, which are located between bands 7 and 8, 19 and 20, 21 and 22, and 23 and 24, respectively. The frequency windows of band gaps I, II, III, and IV are $(0.725, 0.908)$, $(1.182, 1.321)$, $(1.335, 1.409)$, and $(1.451, 1.549)$ with the gap-midgap ratio being 22.4%, 11.1%, 5.4%, and 6.5%, respectively, which are significantly wider than those of multiple band gaps in recently reported SPTIs for TM modes [33], providing possibilities for producing more localized corner states.

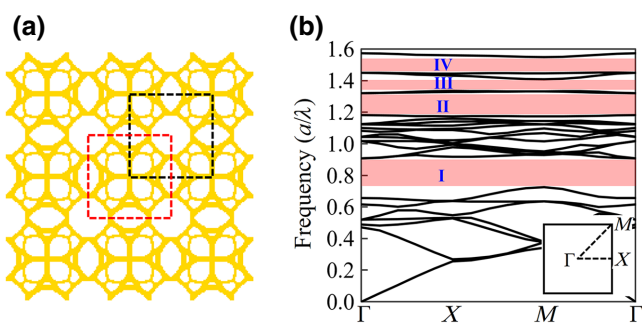


FIG. 1. (a) Optimized PC consisting of 3×3 UCs. (b) The band diagram, where the inset depicts the first irreducible Brillouin zone.

Previous studies on SPTIs engineered in C_{4v} -symmetric lattices indicate that the trivial and nontrivial UCs can be selected from the same PC in different ways [39]. Inspired by this, we choose two kinds of UCs from the optimized PC: one is the primitive UC (UC1), whereas the other one (UC2) is obtained by translating UC1 by $(a/2, a/2)$, denoted by the black dashed box in Fig. 1(a). Next, we use the 2D polarization $\mathbf{P} = (P_x, P_y)$ to characterize the topology properties of UC1 and UC2, which is formulated as [40–42]

$$P_i = \frac{1}{2} \left(\sum_n q_i^n \bmod 2 \right), \quad (-1)^{q_i^n} = \frac{\eta_n(X_i)}{\eta_n(\Gamma)}, \quad (1)$$

where i denotes the x or y axis in the 2D plane. η_n denotes the parity (\pm) at high-symmetry points X or Γ of the n th-order band. The summation $\sum_n q_i^n$ means the summation of q over all the bands below the band gap. Note that using the parities of the bands at high-symmetry points X and Γ to calculate the polarization is much simpler than the approach based on integration of the non-Abelian Berry connection [40–42]. Because UC1 and UC2 obey the C_{4v} point-group symmetry, $P_x = P_y$. Note that the parity at X or Γ can be identified based on the field profiles of corresponding eigenmodes, i.e., the monopolar and quadrupolar modes have an even parity (+), whereas the dipolar mode possesses an odd parity (−). We summarize the parities at X and Γ for bands 1–23 (all bands below band gap IV) in Appendix B. Taking those parities into Eq. (1), we can judge that, for UC1, $\mathbf{P} = (0, 0)$ for band gaps I, II, and III whereas $\mathbf{P} = (1/2, 1/2)$ for band gap IV; for UC2, $\mathbf{P} = (1/2, 1/2)$ for band gaps I, II, and III whereas $\mathbf{P} = (0, 0)$ for bandgap IV. As $\mathbf{P} = (1/2, 1/2)$ and $\mathbf{P} = (0, 0)$ respectively indicate the topological nontrivial and trivial phases, we can get that, for band gaps I–IV, UC1 and UC2 both possess distinct topological properties, ensuring the existence of topological edge modes at the domain wall between them within all band gaps. Meanwhile, the

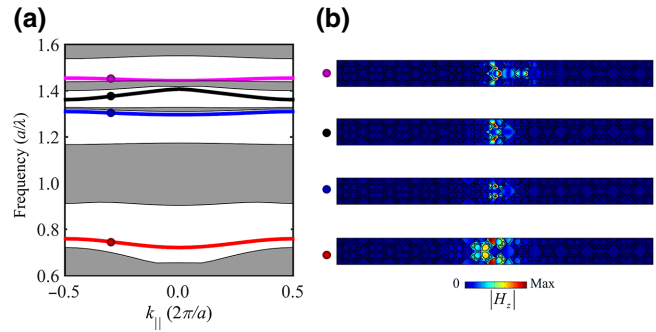


FIG. 2. (a) Projected band diagram of the ribbon structure. (b) The eigenmodes (normalized absolute magnetic field distributions) of the topological edge states at $k = 0.6\pi/a$, corresponding to the colored circles in (a).

topological corner charge, defined by $Q^c = 4P_x P_y$ [40–42], could be induced by the simultaneous nonzero values of P_x and P_y . Therefore, it can be inferred that UC1 and UC2 have different corner charges for band gaps I–IV, guaranteeing the emergence of topological corner states at the 90° corner formed between them within all band gaps.

To verify the multiband topological edge states, we construct a ribbon structure made of six UC1s and six UC2s with a boundary between them, as sketched in Fig. 5(a) in Appendix C. Figure 2(a) shows the calculated band structure of the ribbon structure, from which one can see that four edge states appear within band gaps I–IV, respectively. Figure 2(b) presents the eigenmodes at $k = 0.6\pi/a$ of edge states within band gaps I–IV [corresponding to the colored circles in Fig. 2(a)], demonstrating that energies are highly localized at the boundary between UC1s and UC2s. Importantly, the demonstrated multiband edge states are all gapped, providing room for producing multiband corner states.

Next, we create a SPTI made of 6×6 UC2s surrounded by UC1s with a thickness of $4a$, as sketched in Fig. 5(b) in Appendix C, to validate the multiband topological corner states. Figure 3(a) shows the calculated eigenfrequency spectrum of the SPTI, from which one can observe that four corner states, labeled by C1, C2, C3, and C4, appear within band gaps I, II, III, and IV, respectively, verifying the multiband corner states supported by the designed SPTI. Figure 3(b) plots the absolute magnetic field distributions of the corner states C1–C4, confirming that the energies are indeed localized at the corner. Note that corner state C3 is less localized than the other corner states because its frequency is close to the bottom boundary of band gap III.

Finally, we demonstrate the robustness of the multiband topological corner states by introducing several impurities into the SPTI. As sketched in Fig. 5(c) in Appendix C, the

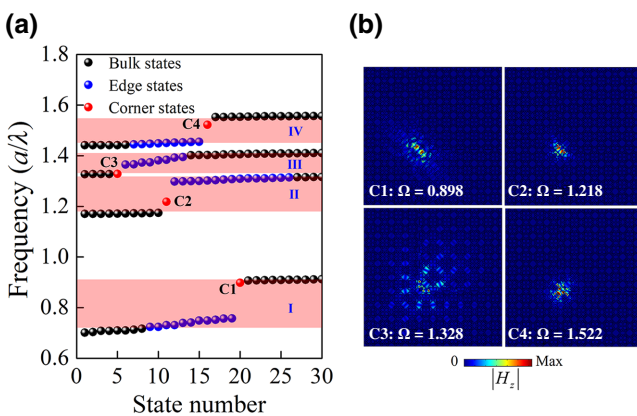


FIG. 3. (a) Calculated eigenfrequency spectrum of the SPTI. (b) Normalized absolute magnetic field distributions of the corner states labeled in (a).

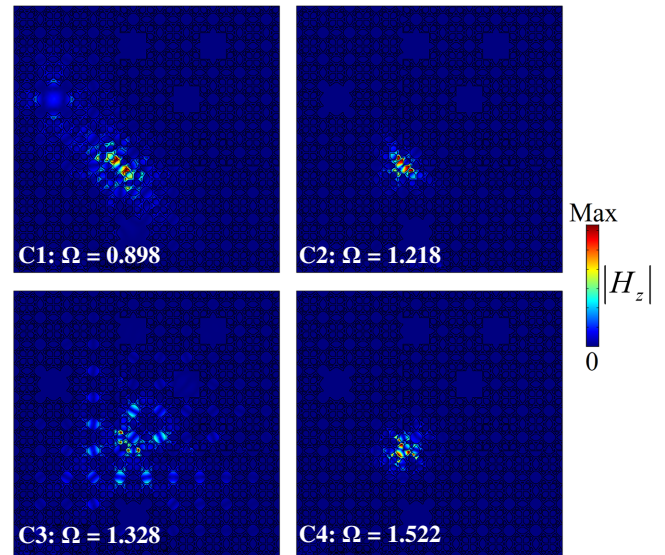


FIG. 4. Normalized absolute magnetic field distributions of the corner states C1–C4 supported by the SPTI with defects.

defects are introduced by removing the dielectric materials within UCs denoted by the red circles. Figure 4 presents the eigenmode profiles of the corner states hosted by the SPTI with defects. We can find that, compared with the corner states of the intact system shown in Fig. 3(b), the eigenfrequencies of all corner states keep invariant although defects are introduced, verifying that the multiband topological corner states are robust against defects.

III. CONCLUSIONS

In summary, toward multiband on-chip optical applications, we design a SPTI that hosts multiband corner states with the aid of the inverse design approach. Totally, four tightly localized corner states are observed within four sizeable band gaps, whose robustness against defects is further demonstrated. Most importantly, the designed SPTI consists of fully connected dielectric materials, which has several advantages in practical applications: it can be readily manufactured at the nanoscale using the method of electron-beam lithography; it can be straightforwardly connected to a waveguide for the ease of exciting and detecting the corner states; it can also be easily coupled into photonic integrated circuits, thus having potential applications in multichannel optical signal processing and communications. Moreover, through the interaction of multiband corner states, the proposed system has great potential in the design of on-chip topological photonic devices with enhanced nonlinear frequency conversion [13,29].

ACKNOWLEDGMENTS

This work is supported by the National Natural Science Foundation of China (No. 1210020421), the Hong Kong Scholars Program (No. XJ2020004), and the Research Grants Council of Hong Kong SAR (Grants No. C6013-18G and No. AoE/P-502/20).

APPENDIX A: TOPOLOGY OPTIMIZATION METHOD

The eigenvalue equation for 2D PCs in TE mode can be formulated as [43,44]

$$-(\nabla + i\mathbf{k}) \cdot \left(\frac{1}{\varepsilon(\mathbf{r})} (\nabla + i\mathbf{k}) H(\mathbf{r}) \right) = \left(\frac{\omega}{c} \right)^2 H(\mathbf{r}), \quad (\text{A1})$$

where $\mathbf{k} = (k_x, k_y)$ represents the Bloch wave vector and $\varepsilon(\mathbf{r})$ and $H(\mathbf{r})$ represent the dielectric constant and the magnetic field at position \mathbf{r} . As Eq. (A1) contains two unknown variables, \mathbf{k} and ω , two methods, $\omega(\mathbf{k})$ and $\mathbf{k}(\omega)$, can be used to solve it. The $\omega(\mathbf{k})$ method solves ω at the given \mathbf{k} and affords the classical band diagram, whereas the $\mathbf{k}(\omega)$ method solves \mathbf{k} at the given ω and affords the complex band diagram [45]. We adopt the $\mathbf{k}(\omega)$ method herein and k_x and k_y are set as $k_x = k \cos \theta$ and $k_y = k \sin \theta$, respectively, where θ denotes the wave vector direction. Using the finite element method, Eq. (A1) could be converted to

$$(k^2 \mathbf{K}_I + k \mathbf{K}_{II} + \mathbf{K}_{III}) \mathbf{u} = \mathbf{0}, \quad (\text{A2})$$

where \mathbf{u} denotes the eigenvector of the magnetic field. The detailed expressions of matrix K_I , K_{II} , and K_{III} can be found in Ref. [44]. Next, to overcome the difficulty of solving the quadratic eigenvalue equation, we convert Eq. (A2) into the standard eigenvalue problem as

$$(\mathbf{K}(\theta, \omega) - k \mathbf{M}(\theta)) \bar{\mathbf{U}} = \mathbf{0}, \quad (\text{A3})$$

where $\mathbf{K} = \begin{bmatrix} \mathbf{K}_{II} & \mathbf{K}_{III} \\ I & \mathbf{0} \end{bmatrix}$, $\mathbf{M} = \begin{bmatrix} -\mathbf{K}_I & \mathbf{0} \\ \mathbf{0} & I \end{bmatrix}$, and $\bar{\mathbf{U}} = \begin{bmatrix} k \mathbf{u} \\ \mathbf{u} \end{bmatrix}$. After solving Eq. (A3) at the specific ω and θ , we can get k in a complex form, $k' + ik''$. Previous work on the complex band structure of PC indicates that, within the

band gap of the classical band structure, all waves become evanescent waves and the minimum k'' is always larger than zero [46]. Therefore, if we maximize the minimum k'' of all wave vector directions at the given frequency, the band gap at this frequency will be automatically opened. And we can get the multiple band gaps by simultaneously maximizing the minimum k'' of all wave vector directions at multiple given frequencies. For a PC with C_{4v} symmetry, $\theta \in [0, \pi/4]$. Therefore, the topology optimization formulation can be expressed by

$$\begin{cases} \max : f(x_e) = \min(k''_{\theta_g, \omega_w}) \\ \text{s.t. : } \theta_g \in \left[0 : \frac{\pi}{16} : \frac{\pi}{4} \right] \\ \omega_w \in (\omega_1, \omega_2, \dots) \\ x_e = 0 \text{ or } 1; e = 1, 2, \dots, m, \end{cases} \quad (\text{A4})$$

where the UC is discretized as m elements and x_e denotes the design variable of the element e , which equals 1 when the element is full of silicon, whereas 0 for air. k''_{θ_g, ω_w} denotes the minimum imaginary part of the wave vector at the specific direction θ_g and frequency ω_w . Totally, four frequencies and ten wave vector directions at each frequency are considered herein. To update the design variables, the sensitivity of each element, i.e., the derivative of the objective function $f(x_e)$ about x_e , should be derived. Differentiating both sides of Eq. (A2), we can get

$$\begin{aligned} & \frac{\partial k''_{\theta_g, \omega_w}}{\partial x_e} \\ &= \text{imag} \left(-\frac{\mathbf{v}^T \left(k_{\theta_g, \omega_w}^2 \frac{\partial \mathbf{K}_I}{\partial x_e} + k_{\theta_g, \omega_w} \frac{\partial \mathbf{K}_{II}}{\partial x_e} + \frac{\partial \mathbf{K}_{III}}{\partial x_e} \right) \mathbf{u}}{2k_{\theta_g, \omega_w} \mathbf{v}^T \mathbf{K}_{II} \mathbf{u} + \mathbf{v}^T \mathbf{K}_{III} \mathbf{u}} \right). \end{aligned} \quad (\text{A5})$$

Upon getting sensitivities of all elements, we start from a random initial structure without any topological band gaps and use the BESO algorithm to iteratively update the design variables [38,44]. BESO increases the design variable of the element with higher sensitivity, $x_e = \min[1, x_e + 0.1]$, and decreases that with lower sensitivity, $x_e = \max[0, x_e - 0.1]$. As a result, a design is constructed with the updated design variables. The finite element analysis and BESO update are repeated until the objective function is maximized [38]. In the optimization, the UC is constrained with C_{4v} symmetry.

TABLE I. Parities at high-symmetry points X and Γ of the band structures for UC1 and UC2.

		Order of band																						
		1	2	3	4	5	6	7	8	9	10	11	12	13	14	15	16	17	18	19	20	21	22	23
UC1	Γ	+	+	+	-	-	+	+	-	-	-	+	+	+	+	-	-	+	+	-	-	-	-	-
	X	-	+	+	-	-	+	-	+	-	+	-	-	-	-	-	-	+	+	+	+	+	+	+
UC2	Γ	+	+	+	-	-	+	+	-	-	-	+	+	+	+	-	-	+	+	+	-	-	-	-
	X	+	-	-	+	+	-	+	-	-	-	+	+	+	-	-	+	+	+	-	-	-	-	-

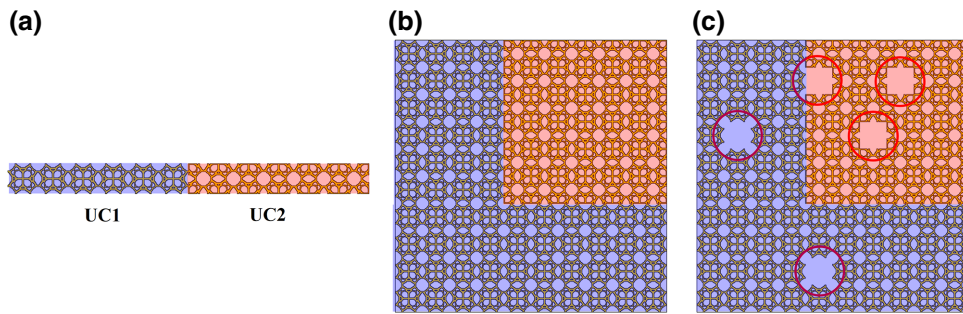


FIG. 5. Schematics of supercells for calculating edge and corner states. (a) The supercell for calculating edge states. (b) The metasstructure for calculating corner states. (c) The metastructure with defects for demonstrating the robustness of corner states. The regions of UC1s and UC2s are denoted by blue and red colors, respectively.

APPENDIX B: PARITIES AT HIGH-SYMMETRY POINTS X AND Γ FOR UC1 AND UC2

Table I gives the parities at high-symmetry points X and Γ of bands 1–23 (below band gap IV) for UC1 and UC2, where the parities with opposite signs are shaded with blue color, which can be taken into Eq. (1) to identify the topological properties of UC1 and UC2.

APPENDIX C: SCHEMATICS OF SUPERCELLS FOR CALCULATING EDGE AND CORNER STATES

Figure 5(a) plots a schematic of the supercell for calculating edge states. Figures 5(b) and 5(c) sketch the metastructure, i.e., SPTI, with and without defects for demonstrating corner states, respectively.

- [1] A. B. Khanikaev and G. Shvets, Two-dimensional topological photonics, *Nat. Photonics* **11**, 763 (2017).
- [2] F. Haldane and S. Raghu, Possible Realization of Directional Optical Waveguides in Photonic Crystals with Broken Time-Reversal Symmetry, *Phys. Rev. Lett.* **100**, 013904 (2008).
- [3] S. Raghu and F. D. M. Haldane, Analogs of quantum-hall-effect edge states in photonic crystals, *Phys. Rev. A* **78**, 033834 (2008).
- [4] L.-H. Wu and X. Hu, Scheme for Achieving a Topological Photonic Crystal by Using Dielectric Material, *Phys. Rev. Lett.* **114**, 223901 (2015).
- [5] D. Smirnova, S. Kruk, D. Leykam, E. Melik-Gaykazyan, D.-Y. Choi, and Y. Kivshar, Third-Harmonic Generation in Photonic Topological Metasurfaces, *Phys. Rev. Lett.* **123**, 103901 (2019).
- [6] Y. Chen, F. Meng, B. Jia, G. Li, and X. Huang, Inverse design of photonic topological insulators with extra-wide bandgaps, *Phys. Status Solidi RRL* **13**, 1900175 (2019).
- [7] X.-T. He, E.-T. Liang, J.-J. Yuan, H.-Y. Qiu, X.-D. Chen, F.-L. Zhao, and J.-W. Dong, A silicon-on-insulator slab for topological valley transport, *Nat. Commun.* **10**, 872 (2019).
- [8] X.-D. Chen, F.-L. Zhao, M. Chen, and J.-W. Dong, Valley-contrasting physics in all-dielectric photonic crystals: orbital angular momentum and topological propagation, *Phys. Rev. B* **96**, 020202 (2017).
- [9] X. Ni, D. Purtseladze, D. A. Smirnova, A. Slobozhanyuk, A. Alù, and A. B. Khanikaev, Spin-and valley-polarized one-way klein tunneling in photonic topological insulators, *Sci. Adv.* **4**, eaap8802 (2018).
- [10] M. Saba, S. Wong, M. Elman, S. S. Oh, and O. Hess, Nature of topological protection in photonic spin and valley hall insulators, *Phys. Rev. B* **101**, 054307 (2020).
- [11] Y. Zeng, U. Chattopadhyay, B. Zhu, B. Qiang, J. Li, Y. Jin, L. Li, A. G. Davies, E. H. Linfield, B. Zhang, Y. Chong, and Q. J. Wang, Electrically pumped topological laser with valley edge modes, *Nature* **578**, 246 (2020).
- [12] Q. Chen, L. Zhang, M. He, Z. Wang, X. Lin, F. Gao, Y. Yang, B. Zhang, and H. Chen, Valley-Hall photonic topological insulators with dual-band kink states, *Adv. Opt. Mater.* **7**, 1900036 (2019).
- [13] Z. Lan, J. W. You, Q. Ren, W. E. I. Sha, and N. C. Panoiu, Second-harmonic generation via double topological valley-hall kink modes in all-dielectric photonic crystals, *Phys. Rev. A* **103**, L041502 (2021).
- [14] B. Xie, H.-X. Wang, X. Zhang, P. Zhan, J.-H. Jiang, M. Lu, and Y. Chen, Higher-order band topology, *Nat. Rev. Phys.* **3**, 520 (2021).
- [15] B. Xie, G. Su, H.-F. Wang, F. Liu, L. Hu, S.-Y. Yu, P. Zhan, M.-H. Lu, Z. Wang, and Y.-F. Chen, Higher-order quantum spin Hall effect in a photonic crystal, *Nat. Commun.* **11**, 3768 (2020).
- [16] Y. Chen, F. Meng, Y. Kivshar, B. Jia, and X. Huang, Inverse design of higher-order photonic topological insulators, *Phys. Rev. Res.* **2**, 023115 (2020).
- [17] H.-X. Wang, L. Liang, B. Jiang, J. Hu, X. Lu, and J.-H. Jiang, Higher-order topological phases in tunable C3 symmetric photonic crystals, *Photonics Res.* **9**, 1854 (2021).
- [18] M. Li, D. Zhirihi, M. Gorlach, X. Ni, D. Filonov, A. Slobozhanyuk, A. Alù, and A. B. Khanikaev, Higher-order topological states in photonic kagome crystals with long-range interactions, *Nat. Photonics* **14**, 89 (2020).
- [19] X.-D. Chen, W.-M. Deng, F.-L. Shi, F.-L. Zhao, M. Chen, and J.-W. Dong, Direct Observation of Corner States in Second-Order Topological Photonic Crystal Slabs, *Phys. Rev. Lett.* **122**, 233902 (2019).

- [20] B.-Y. Xie, H.-F. Wang, H.-X. Wang, X.-Y. Zhu, J.-H. Jiang, M.-H. Lu, and Y.-F. Chen, Second-order photonic topological insulator with corner states, *Phys. Rev. B* **98**, 205147 (2018).
- [21] B.-Y. Xie, G.-X. Su, H.-F. Wang, H. Su, X.-P. Shen, P. Zhan, M.-H. Lu, Z.-L. Wang, and Y.-F. Chen, Visualization of Higher-Order Topological Insulating Phases in Two-Dimensional Dielectric Photonic Crystals, *Phys. Rev. Lett.* **122**, 233903 (2019).
- [22] L. Zhang, Y. Yang, Z.-K. Lin, P. Qin, Q. Chen, F. Gao, E. Li, J.-H. Jiang, B. Zhang, and H. Chen, Higher-order topological states in surface-wave photonic crystals, *Adv. Sci.* **7**, 1902724 (2020).
- [23] X. Zhou, Z.-K. Lin, W. Lu, Y. Lai, B. Hou, and J.-H. Jiang, Twisted quadrupole topological photonic crystals, *Laser Photonics Rev.* **14**, 2000010 (2020).
- [24] Y. Chen, F. Meng, Z. Lan, B. Jia, and X. Huang, Dual-Polarization Second-Order Photonic Topological Insulators, *Phys. Rev. Appl.* **15**, 034053 (2021).
- [25] Y. Ota, F. Liu, R. Katsumi, K. Watanabe, K. Wakabayashi, Y. Arakawa, and S. Iwamoto, Photonic crystal nanocavity based on a topological corner state, *Optica* **6**, 786 (2019).
- [26] W. Zhang, X. Xie, H. Hao, J. Dang, S. Xiao, S. Shi, H. Ni, Z. Niu, C. Wang, K. Jin, X. Zhang, and X. Xu, Low-threshold topological nanolasers based on the second-order corner state, *Light Sci. Appl.* **9**, 109 (2020).
- [27] H.-R. Kim, M.-S. Hwang, D. Smirnova, K.-Y. Jeong, Y. Kivshar, and H.-G. Park, Multipolar lasing modes from topological corner states, *Nat. Commun.* **11**, 5758 (2020).
- [28] S. S. Kruk, W. Gao, D.-Y. Choi, T. Zentgraf, S. Zhang, and Y. Kivshar, Nonlinear imaging of nanoscale topological corner states, *Nano Lett.* **21**, 4592 (2021).
- [29] Y. Chen, Z. Lan, J. Li, and J. Zhu, Topologically protected second harmonic generation via doubly resonant high-order photonic modes, *Phys. Rev. B* **104**, 155421 (2021).
- [30] K. Guesmi, L. Abdeladim, S. Tozer, P. Mahou, T. Kumamoto, K. Jurkus, P. Rigaud, K. Loulier, N. Dray, and P. Georges, Dual-color deep-tissue three-photon microscopy with a multiband infrared laser, *Light Sci. Appl.* **7**, 1 (2018).
- [31] O. Turkmen, E. Ekmekci, and G. Turhan-Sayan, Nested U-ring resonators: A novel multi-band metamaterial design in microwave region, *IET Microw. Antennas Propag.* **6**, 1102 (2012).
- [32] G. Shambat, M. S. Mirotznik, G. W. Euliss, V. Smolski, E. G. Johnson, and R. A. Athale, Photonic crystal filters for multi-band optical filtering on a monolithic substrate, *J. Nanophotonics.* **3**, 031506 (2009).
- [33] K. H. Kim and K. K. Om, Multiband photonic topological valley-Hall edge modes and second-order corner states in square lattices, *Adv. Opt. Mater.* **9**, 2001865 (2021).
- [34] J. Ma, X. Xi, and X. Sun, Topological photonic integrated circuits based on valley kink states, *Laser Photonics Rev.* **13**, 1900087 (2019).
- [35] B. Shen, P. Wang, R. Polson, and R. Menon, An integrated-nanophotonics polarization beamsplitter with $2.4 \times 2.4 \mu\text{m}^2$ footprint, *Nat. Photonics* **9**, 378 (2015).
- [36] A. Y. Piggott, J. Lu, K. G. Lagoudakis, J. Petykiewicz, T. M. Babinec, and J. Vučković, Inverse design and demonstration of a compact and broadband on-chip wavelength demultiplexer, *Nat. Photonics* **9**, 374 (2015).
- [37] O. Sigmund and K. Hougard, Geometric Properties of Optimal Photonic Crystals, *Phys. Rev. Lett.* **100**, 153904 (2008).
- [38] X. Huang and Y. Xie, *Evolutionary Topology Optimization of Continuum Structures: Methods and Applications* (John Wiley & Sons, Hoboken, New Jersey, 2010).
- [39] Y. Chen, Z. Lan, and J. Zhu, Second-order topological phases in C_{4v} -symmetric photonic crystals beyond the two-dimensional Su-Schrieffer-Heeger model, *Nanophotonics* **11**, 1345 (2022).
- [40] F. Liu, H.-Y. Deng, and K. Wakabayashi, Helical Topological Edge States in a Quadrupole Phase, *Phys. Rev. Lett.* **122**, 086804 (2019).
- [41] Z. Zhang, M. R. López, Y. Cheng, X. Liu, and J. Christensen, Non-Hermitian Sonic Second-Order Topological Insulator, *Phys. Rev. Lett.* **122**, 195501 (2019).
- [42] Z. Zhang, H. Long, C. Liu, C. Shao, Y. Cheng, X. Liu, and J. Christensen, Deep-subwavelength holey acoustic second-order topological insulators, *Adv. Mater.* **31**, 1904682 (2019).
- [43] J. D. Joannopoulos, S. G. Johnson, J. N. Winn, and R. D. Meade, *Photonic Crystals: Molding the Flow of Light* (Princeton University Press, Princeton, New Jersey, 2011).
- [44] Y. Chen, F. Meng, G. Li, and X. Huang, Designing photonic materials with complete band gaps by topology optimization, *Smart Mater. Struct.* **28**, 015025 (2018).
- [45] V. Laude, J. M. Escalante, and A. Martínez, Effect of loss on the dispersion relation of photonic and phononic crystals, *Phys. Rev. B* **88**, 224302 (2013).
- [46] M. Botey, Y.-C. Cheng, V. Romero-Garcia, R. Picó, R. Herrero, V. Sánchez-Morcillo, and K. Staliunas, Unlocked evanescent waves in periodic structures, *Opt. Lett.* **38**, 1890 (2013).